scientific reports

Check for updates

OPEN

Broadband bifunctional Luneburg–Fisheye lens based on anisotropic metasurface

Jiaqing Chen✉, Yongjiu Zhao✉, Lei Xing, Zheng He & Luyang Sun

Luneburg lenses and Maxwell fisheye lenses possess distinct properties of focusing, well beyond conventional lenses made of uniform materials. In this paper, a planar broadband bifunctional Luneburg-fisheye lens synthesized by gradient anisotropic metasurface is proposed. The proposed anisotropic metasurface is formed by non-resonant anisotropic cells, so that it can independently realize the equivalent gradient refractive indexes of Luneburg lens and Maxwell fisheye lens along orthogonal directions in a broad band, respectively. To verify the performance of the bifunctional lens, a prototype associated with a feeding log-periodic dipole antenna has been fabricated. Experimental results show that the proposed lens functions well over a wide frequency range with high efficiency and low profile, which coincides well with theoretical predictions and simulated results. It is expected that the proposed design will facilitate the applications of multifunctional metadevices in microwave and optical ranges.

In the past decade, metasurfaces, by virtue of their fantastic physical characteristics associated with ultrathin configurations, have attracted an extensive interest in the fields of microwave, optics, and even acoustics[1–3]. Following the proposal of the generalized Snell's laws of reflection and refraction[4,5], gradient metasurfaces have proven to be an unprecedented approach to manipulating the propagation of electromagnetic (EM) waves. Since then, a range of revolutionary functionalities have been realized, such as beam steering[6–8], invisibility cloaks[9], polarization rotators[10], vortex phase plates[11,12], and flattened gradient lenses[13–15].

As alternatives to conventional lenses, gradient refractive index (GRIN) lenses constructed by inhomogeneous artificially structured metasurfaces can achieve significant reductions in volume and weight, facilitating the integration with other microwave or optical devices[15]. Furthermore, benefiting from the elimination of wave font aberration, metasurface-based gradient lenses are more capable for highly-directional emission with low loss[13,16–20]. Among the GRIN lenses, Luneburg lens and Maxwell Fisheye lens have come into prominence recently and become more and more indispensable in collimating lights, wide-angle cameras, and communication systems due to their distinct properties of focusing[21].

Luneburg lens is a typical GRIN lens with spherical symmetry, whose refractive index varies gradually from at the center to 1 on the outermost shell. Theoretically, it is able to guide the incoming plane wave from arbitrary directions to a focal point on the opposite surface of the lens without aberration (or vice versa). Similarly, Maxwell Fisheye lens is a spherically symmetric GRIN lens as well, whose refractive index decreases radially from 2 at the center to 1 on the perimeter in general. It can focus the radiation emitted from a point source to a diametrically opposite point on the lens rim.

Despite the ease of fabrication and superior performance, most of the Luneburg lenses or Maxwell fisheye lenses designed previously by metamaterials still suffer from bulk configurations[22–26]. Planar Luneburg lenses or fisheye lenses can effectively lower the profile of the whole structure, while maintaining the radiation characteristics. However, most of the flat metalenses in contemporary works could hardly adjust the distributions of the refractive index along two polarization directions independently[27–32], namely that most of them are isotropic and serving as single-function devices. Resulting from the demand for miniaturization and multifunction of microwave or optical devices, integration of multiple functions has been brought into focus. As we know, anisotropic metasurfaces (AMs) can manipulate orthogonally polarized waves independently with high efficiency[33], which would be a promising candidate for the design of multifunctional metalens. Hence, gradient anisotropic metasurface (GAM), which can achieve different gradient distributions of refractive index along orthogonal directions, is evolved. By adjusting the geometrical parameters of the GAMs, bifunctional metalenses, combining the function of a Luneburg lens and that of a fisheye lens, are presented[21,34,35]. While, the bandwidths of the

College of Electronic and Information Engineering, Nanjing University of Aeronautics and Astronautics, Nanjing 211100, China. ✉email: yzcnchen@foxmail.com; yjzhao@nuaa.edu.cn

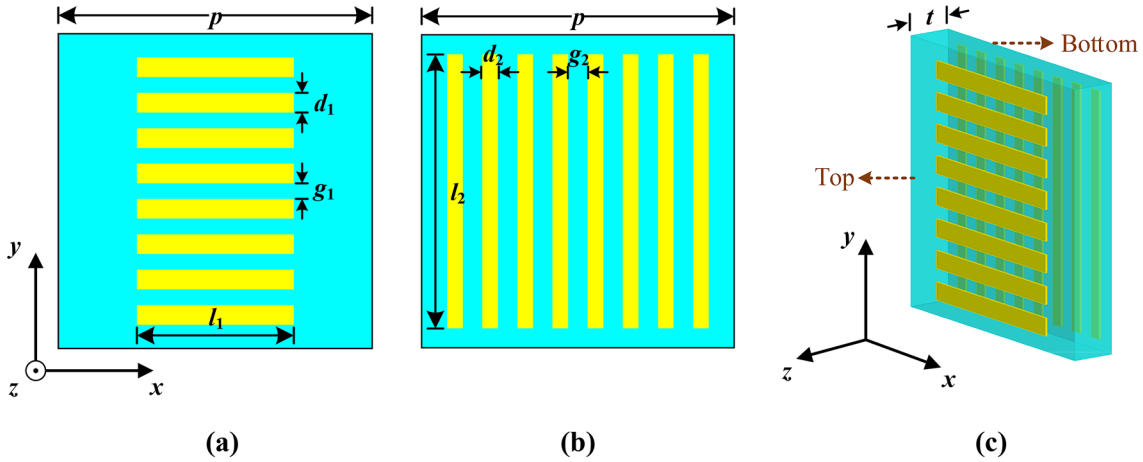

Figure 1. Configuration of the proposed anisotropic cell. (**a**) Top view. (**b**) Bottom view. (**c**) Perspective view.

lenses mentioned above are extremely restricted because of the intrinsic resonance characteristics of the AMs and the coupling between adjacent cells.

In this paper, a broadband bifunctional Luneburg-fisheye lens constructed by gradient anisotropic metasurface (GAM) is proposed, which characters as a Luneburg lens viewing from the horizontal axis in the frequency range of 2 to 8 GHz (relative bandwidth of 120%), while as a Maxwell fisheye lens viewing from the vertical axis in the band of 5 to 7 GHz (relative bandwidth of 33.3%). The proposed design of the Luneburg-fisheye lens stands out from the aforementioned designs in three aspects. First, the proposed metalens can achieve a bifunctional response of a Luneburg lens and a fisheye lens over a broad band far beyond the existing designs. The constitutive GAM is synthesized by non-resonant anisotropic cells applying with quasi-conformal mapping method, so that it can independently regulate the inhomogeneous refractive-index distributions in two orthogonal directions. Second, the bifunctional lens is designed to be flattened with compact size and low loss, resulting in easy integration with other devices. Third, what needs to be highlighted is that this anisotropy-based approach is not limited to a combination of the two lenses. It can be flexibly extended to the realization of other broadband bifunctional metadevices, such as Luneburg-Eaton lens, Eaton-fisheye lens, and so on.

Results

Design and analysis of the anisotropic unit cell. The configuration of the proposed anisotropic unit cell used for the synthesis of the bifunctional lens is demonstrated in Fig. 1. The anisotropic cell consists of two mutually orthogonal parallel-line arrays. The two sets of the metallic array are attached separately on both sides of a commercial F4B substrate ($\varepsilon_r = 2.2$, $\tan\delta = 0.001$) with a thickness of $t = 1$ mm (0.027λ at 8 GHz). Considering the operating band of the metalens, the periodicity p of the anisotropic cell is set as 6 mm.

As mentioned above, it is extremely difficult to realize a bifunctional lens with isotropic materials. Here, we will discuss the feasibility of realizing a Luneburg-fisheye lens with anisotropic metasurface (AM). Suppose that a point source is located on xoy-plane to illuminate the synthesized metalens, which is inhomogeneous, as shown in Fig. 2. When the EM wave emitted from the point source travels along x axis, the refractive index of the cell block is denoted as n_x (like Unit A). Similarly, when the EM wave propagates along y axis, the refractive index of the cell block is denoted as n_y. In the case of oblique incidence with an angle of θ relative to the x-axis, we rotate the former coordinates counterclockwise by the angle of θ so that a new coordinate system can be formed, marked by x'-y' axes, as depicted in Unit B. The coordinate transformation resulting from the rotation can be expressed as follows:

$$\begin{cases} x' = x\cos\theta + y\sin\theta \\ y' = y\cos\theta - x\sin\theta \end{cases} \tag{1}$$

With respect to the new coordinate system, the refractive index tensor of the cell block can be calculated by the following expression.

$$\begin{cases} n_{x'x'} = n_x\cos^2\theta + n_y\sin^2\theta \\ n_{y'y'} = n_x\sin^2\theta + n_y\cos^2\theta \\ n_{x'y'} = n_{y'x'} = (n_y - n_x)\sin\theta\cos\theta \end{cases} \tag{2}$$

As we know, to realize a bifunctional metalens, the metasurface should be anisotropic in orthogonal directions (i.e. x- and y-axis). While, the AM is also expected to remain nearly isotropic along each axis under the circumstance of oblique incidence. As indicated by expression (2), when the incident angle θ is small, $n_{x'x'}$ and $n_{y'y'}$ is approximately equal to n_x and n_y, respectively. Furthermore, the cross-polarization components $n_{x'y'}$ and $n_{y'x'}$ are approaching zero in this case. However, if θ is getting larger, the preceding conclusions will only be applicable when the values of n_x and n_y are close to each other. According to the previous descriptions of the Luneburg lens

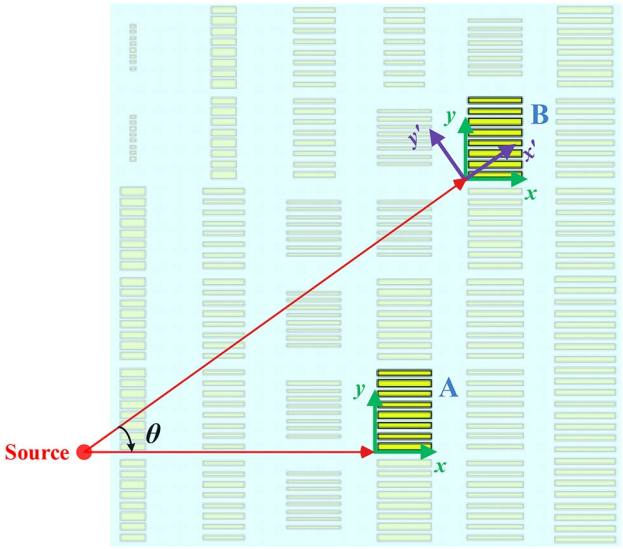

Figure 2. A fraction of the synthesized lens based on anisotropic cells (Top View).

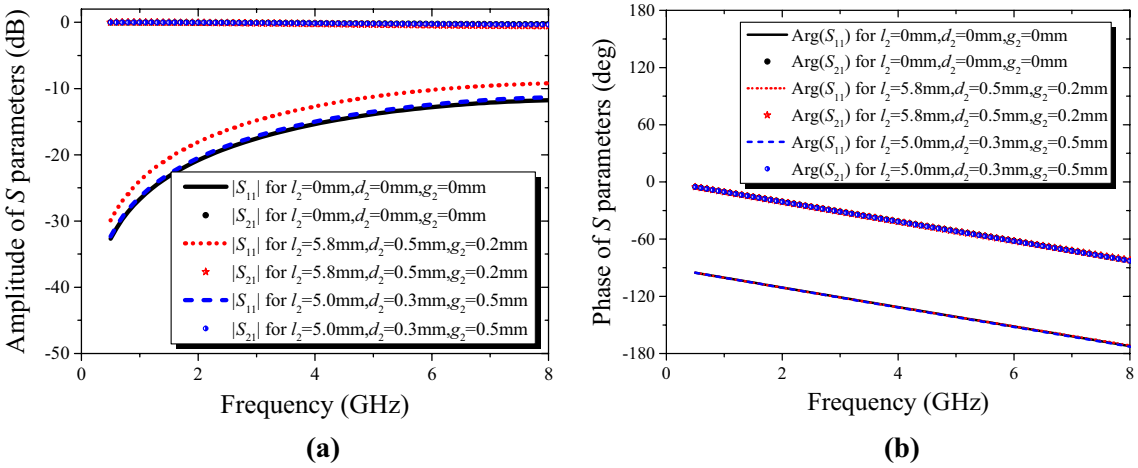

Figure 3. Variations of *S* parameters for the proposed anisotropic cells with different bottom dimensions ($l_1 = 4$ mm, $d_1 = 0.35$ mm, $g_1 = 0.4$ mm). (**a**) Amplitude variation of *S* parameters. (**b**) Phase variation of *S* parameters.

and Maxwell Fisheye lens, the variation range of the refractive index can be characterized as $[1,\sqrt{2}]$ and [1, 2], respectively. Hence, the farther away from the center of the lens, which is corresponding to the increasing of θ, the closer the values of the refractive index will be in orthogonal directions. In other words, when θ is large, the deviation value between n_x and n_y could be very small. Thus, $n_{x'x'}$ and $n_{y'y'}$ can still approximate to n_x and n_y, respectively, and the cross couplings can also be diminished (i.e. $n_{x'y'} \approx n_{y'x'} \approx 0$). In brief, the values of n_x and n_y can be modulated independently for small incident angles; whereas the values of n_x and n_y should be designed approximately identical for the situations of large-angle incidence. From the analyses above, it is feasible to fulfill the requirements of a Luneburg-fisheye lens with an AM theoretically, applying the quasi-conformal mapping method[29,36].

To further validate the anisotropy of the proposed unit cell, the characteristics of the anisotropic cell are simulated by commercial software of CST Microwave Studio Suite. Provided that *x*-polarized incident waves propagate along *y*-axis as shown in Fig. 1, the variations of transmission and reflection coefficient versus frequency are plotted in Fig. 3. As can be seen from Fig. 3, despite changing the geometrical dimensions of the bottom structure arbitrarily, the differences between the values of S_{11} or S_{21} could be tiny, as long as the top structure remains unchanged (i.e. l_1, d_1, and g_1 are fixed). Conversely, similar results will be achieved, given that the structure of the top and the bottom metallic layers is similar but oriented orthogonally. Obviously, the proposed unit cell can be anisotropic and the EM responses along *x*- and *y*-axis can be regulated independently as well. Moreover, magnitudes of the transmission coefficient S_{21} are all close to 0 in Fig. 3, indicating high transmission of the proposed AM (≥ 0.9).

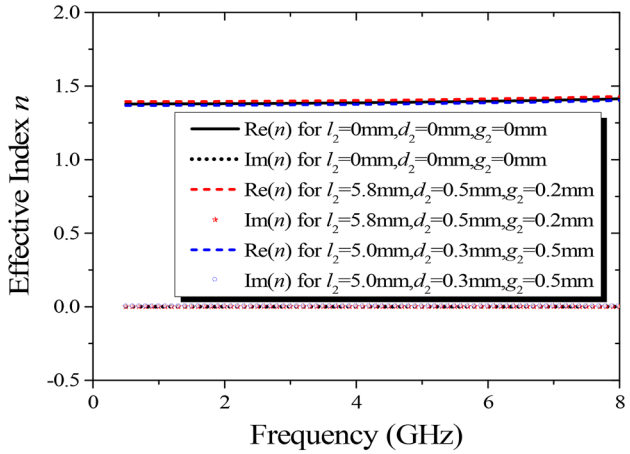

Figure 4. Variations of effective refractive index versus frequency when the dimensions of the top structure are fixed ($l_1 = 4$ mm, $d_1 = 0.35$ mm, $g_1 = 0.4$ mm).

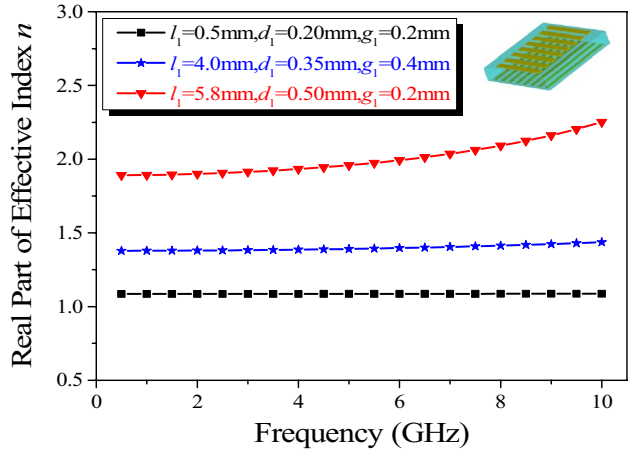

Figure 5. Variations of effective refractive index versus frequency when the dimensions of the bottom structure are fixed.

Applying effective medium theory, the effective refractive index of the proposed anisotropic cells can be retrieved by a *S*-parameter inversion method[37,38,39]. According to the correlative reflection and transmission coefficient shown in Fig. 3, the variations of effective refractive index for different bottom structural dimensions are displayed in Fig. 4. If the dimensions of top structure remain invariable, the effect on the retrieved parameters will be negligible, regardless of the sizes of the bottom structure, and the values of the effective refractive index are nearly constant in a wide frequency range as expected. In addition, the imaginary part of the extracted refractive index is roughly equal to 0, signifying low loss of the proposed lens.

Another difficulty of realizing a broadband Luneburg-fisheye lens lies in the coverage of the effective refractive index. As can be seen from Fig. 3, the proposed anisotropic cell operates in a non-resonant region, leading to an inherently broadband property and low loss. Since the structure of the top layer is similar to that of the bottom layer, and the refractive index distributions in orthogonal directions can be adjusted independently, the refractive indexes of the anisotropic cells with varying structural parameters are extracted when the values of l_2, d_2, and g_2 are fixed, as shown in Fig. 5. The variations of the effective refractive indexes versus frequency are minor, and by varying the geometries of the proposed anisotropic cell, the requirements of the refractive index distribution for the two lenses can be achieved in a wide band. The detailed variations of structural parameters are listed in Table 1. Accordingly, the corresponding values of the effective refractive index n_x for Luneburg lens can range from 1.04 to 1.40 in the band of 2 to 8 GHz, while, that of n_y for Maxwell fisheye lens can range from 1.04 to 1.99 in the band of 5 to 7 GHz.

Design of the bifunctional Luneburg-fisheye lens. Sequel to the characteristics of the anisotropic cell, a broadband Luneburg-fisheye lens can be synthesized based on the specified refractive-index distributions of the two lenses.

The refractive index distribution of the Luneburg lens satisfies the following function of spatial position:

Parameter	Value	Parameter	Value
l_1	0.5–4.0	l_2	0.5–5.8
d_1	0.2–0.5	d_2	0.2–0.5
g_1	0.2–0.4	g_2	0.2–0.5

Table 1. Geometry parameter variations of the proposed anisotropic cell (unit: mm).

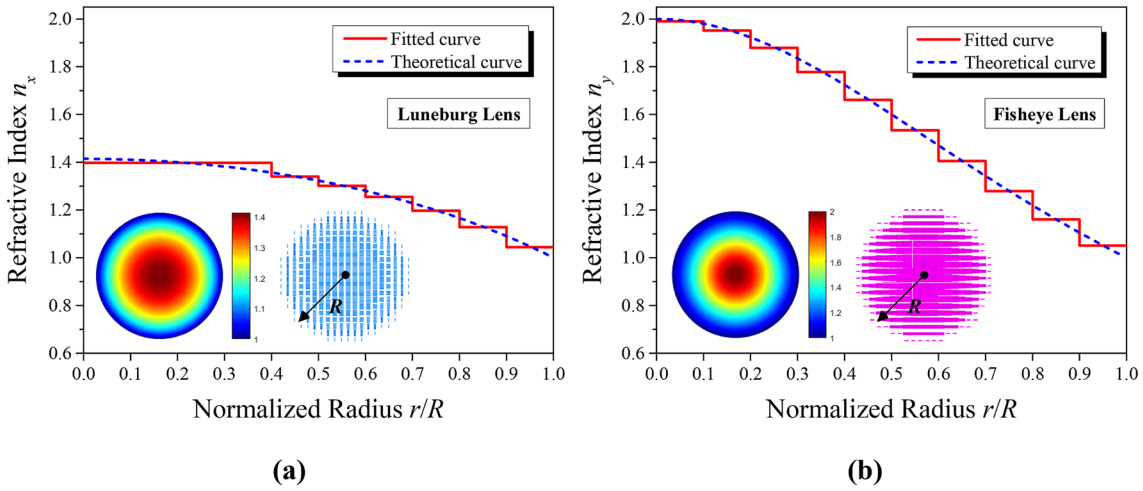

Figure 6. Comparison of the refractive index profiles between the theoretical and fitting distribution. In each graph, the left inset describes the ideal distribution of refractive index, and the right one exhibits the practical schematic of the synthesized lens. (**a**) Mapping of the Luneburg lens (top view). (**b**) Mapping of the Maxwell fisheye lens (bottom view).

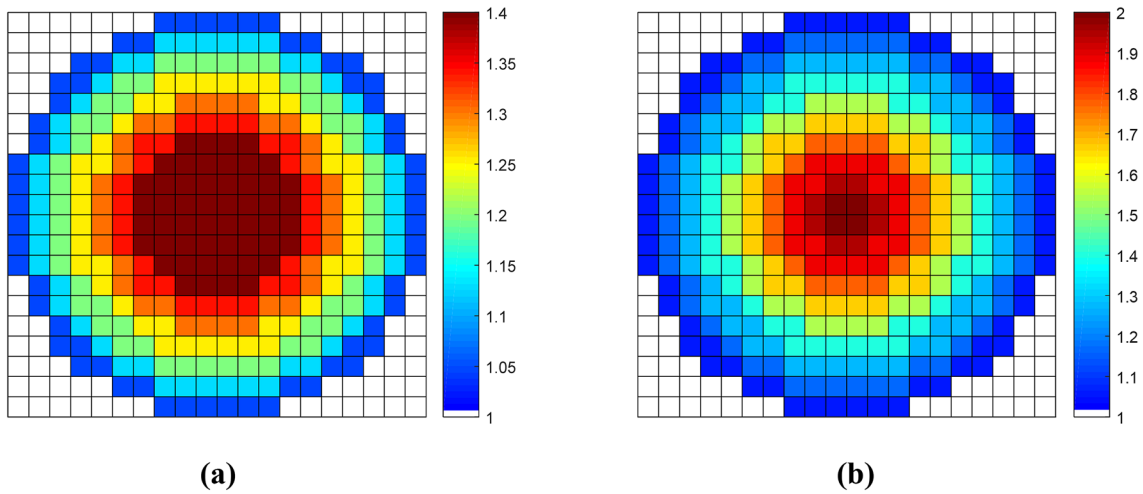

Figure 7. Discretized distribution of the refractive index. (**a**) Mapping of the Luneburg lens. (**b**) Mapping of the Maxwell fisheye lens.

$$n_x(r) = \sqrt{2 - (r/R)^2}, (0 \le r \le R) \tag{3}$$

where R is the radius of the lens, as shown in Fig. 6, and r is the radial distance away from the center of the lens. The refractive index distribution of the Maxwell fisheye lens obeys:

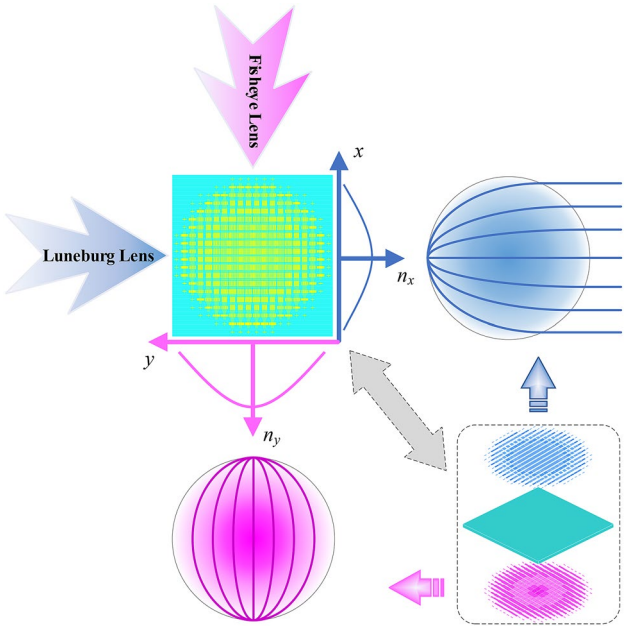

Figure 8. Illustration of the bifunctional Luneburg-fisheye lens synthesized by the proposed anisotropic cells.

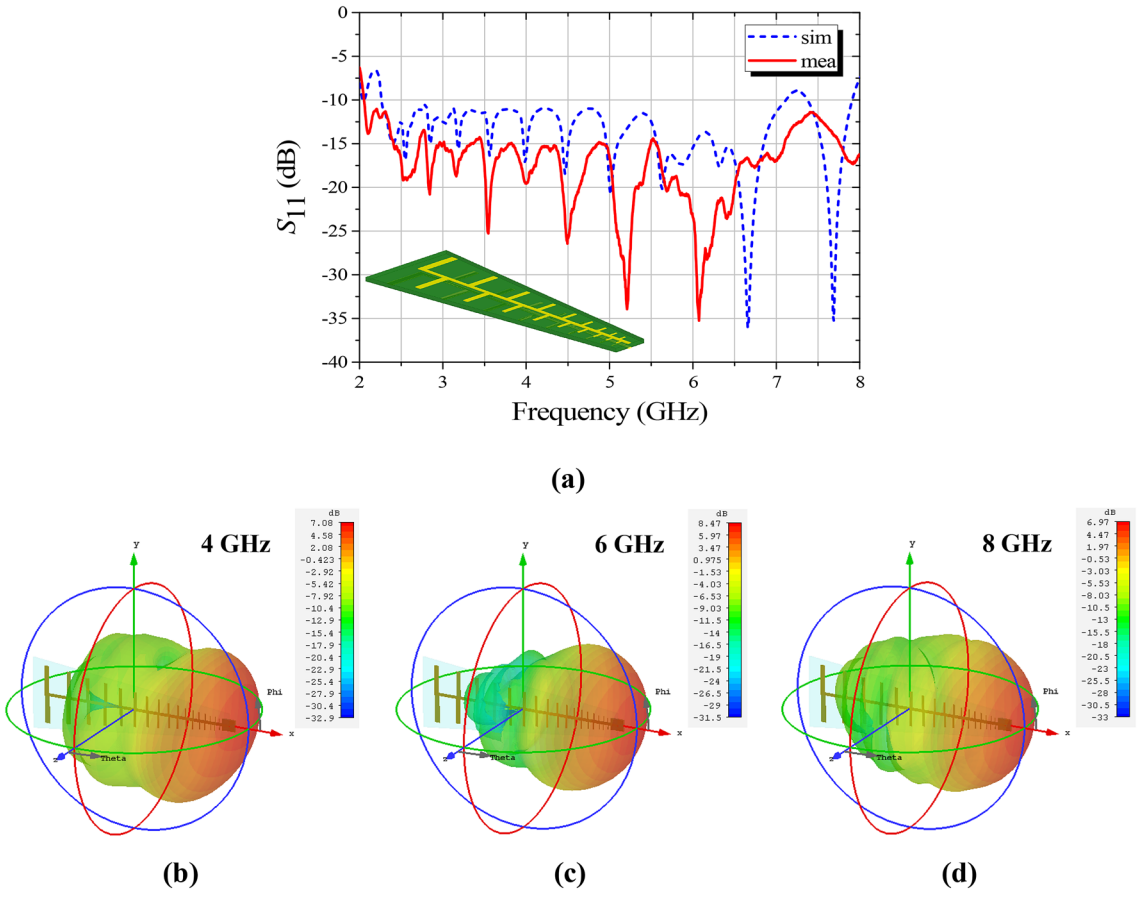

Figure 9. The performance of the feeding LPDA. (**a**) Simulated and measured S_{11} of the LPDA. The inset on the lower left is the model of the proposed LPDA. (**b**) 3-D radiation pattern of the LPDA at 4 GHz. (**c**) 3-D radiation pattern of the LPDA at 6 GHz. (**d**) 3-D radiation pattern of the LPDA at 8 GHz.

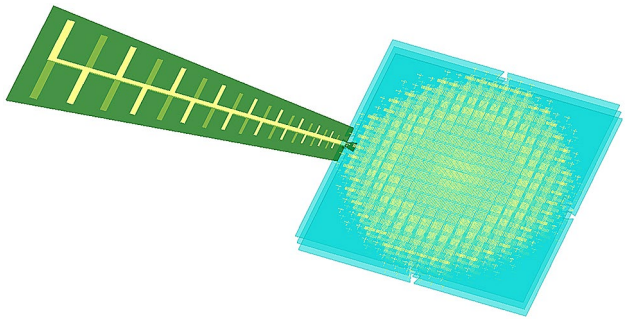

Figure 10. Schematic diagram of the whole system after assembly.

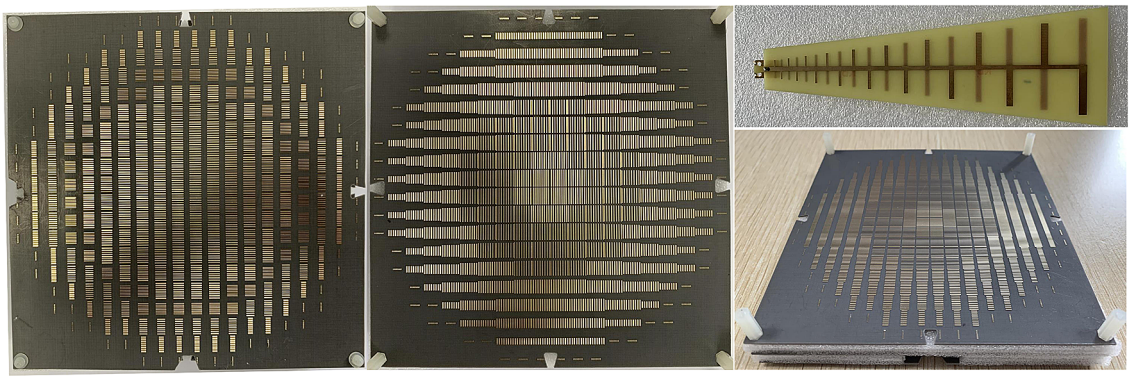

(a)

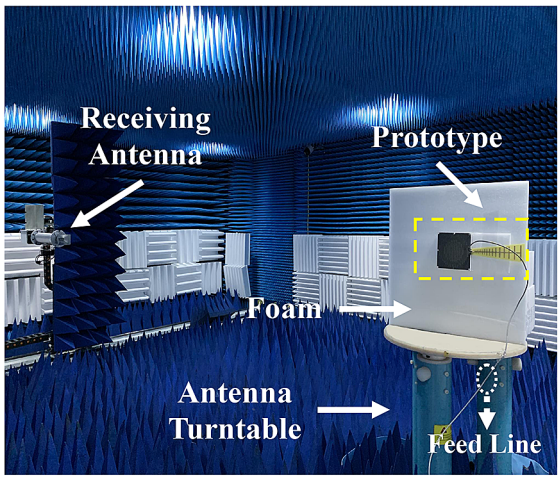

(b)

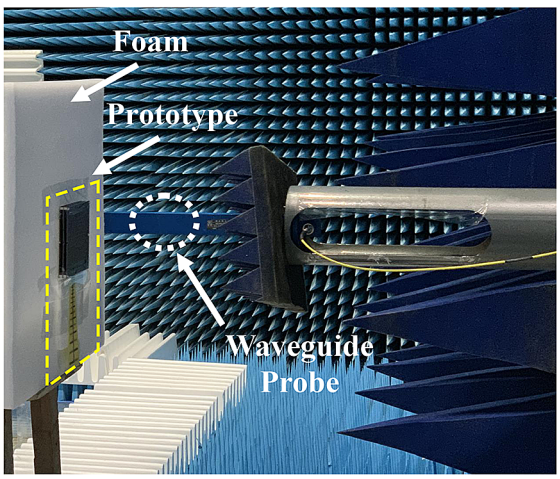

(c)

Figure 11. Photograph of the fabricated prototype and the experimental setup. (**a**) Prototypes of the Luneburg lens (top structure), the Maxwell fisheye lens (bottom structure), the feeding LPDA, and tri-layered metalens after assembly (from left to right). (**b**) Far-field setup. (**c**) Near-field setup.

$$n_y(r) = n_0/[1 + (r/R)^2], (0 \le r \le R) \tag{4}$$

Here, R is the radius of the lens, and r is the radial coordinate as well. n_0 represents the maximum refractive index at the center of the lens, whose value is set as 2 generally.

As demonstrated in Fig. 6, stepped refractive index profiles are employed to approximate the theoretical ones calculated by (3) and (4). In order to integrate the functions of the two lenses into a single dielectric slab, an anisotropic metasurface consists of 20×20 cell blocks is designed, whose overall size is 120 mm × 120 mm × 1 mm (i.e. $3.2\lambda \times 3.2\lambda \times 0.027\lambda$ at 8 GHz). The discretized refractive-index distributions of the two lenses are displayed

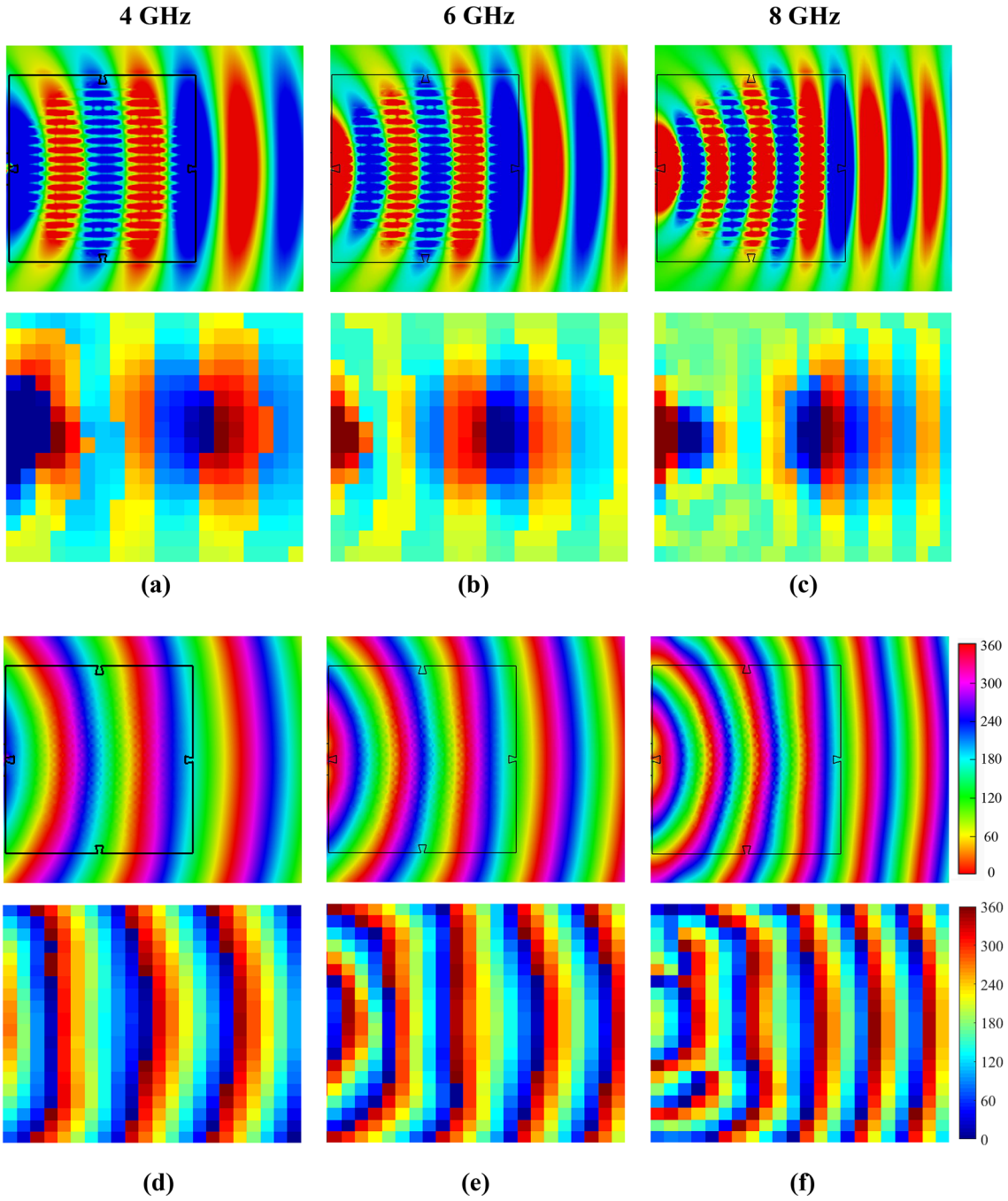

Figure 12. Comparisons of near electric-field distributions (E_x) on *xoy*-plane between the simulated results (upper part of each subgraph) and measured results (bottom part of each subgraph) at 4, 6, and 8 GHz when the proposed bifunctional metalens serves as a Luneburg lens. (**a,b,c**) Amplitude distributions of simulated and measured electric field at 4, 6, and 8 GHz, respectively. (**d,e,f**) Phase distributions of simulated and measured electric field at 4, 6, and 8 GHz, respectively.

in Fig. 7, based on a method of quasi-conformal mapping. For practical implementation, the Luneburg lens and the fisheye lens is finally discretized into seven and ten concentric circular regions, respectively.

Once the dimensions of the filling cells are ascertained in accordance with the refractive index distributions arranged in Fig. 7, a broadband bifunctional Luneburg-fisheye lens can be realized, as shown in Fig. 8. It can be seen clearly that the synthesized AM behaves as a Luneburg lens viewing from the horizontal orientation, while behaves as a Maxwell fisheye lens viewing from the vertical orientation. The metasurface on the top layer corresponds to the Luneburg lens (blue part), and the one on the bottom layer corresponds to the fisheye lens (pink part). Under the illumination of orthogonally polarized waves, the two lenses can achieve their distinct functions of beam focusing independently (see the blue and pink ray tracing, respectively).

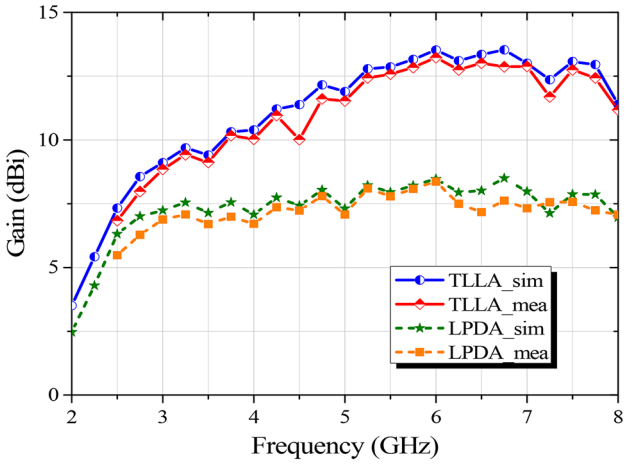

Figure 13. Comparison of the simulated and measured gains versus frequency when the proposed metalens serves as a Luneburg lens.

Simulated and experimental results of the bifunctional lens. In consideration of the demand for broadband response and miniaturization, a planar log-periodic dipole antenna (LPDA) is designed as the feeding source, as shown in Fig. 9a. With which, the bifunctional Luneburg-fisheye lens can be excited by directional TE-mode surface waves, fulfilling the requirement of the proposed AM. The LPDA is printed on a commercial FR4 substrate ($\varepsilon_r = 4.4$, and tan $\delta = 0.02$) with a thickness of 1 mm. The impedance characteristic (S_{11}) and the radiation performance of the LPDA is detailedly presented in Fig. 9, respectively. As shown, the designed LPDA roughly operates over a wide frequency range from 2 to 8 GHz, and exhibits a desired performance of directional radiation along the central axis (see Fig. 9b–d).

Aiming to improve the performance of the proposed bifunctional lens, a triple-layered structure is adopted, and the stacking AMs are spaced 6 mm apart from each other. The schematic diagram of the whole system after assembly is demonstrated in Fig. 10. Specifically, the feeding LPDA is coplanar with the middle AM, locating on the periphery of the metalens, and the central axis of the LPDA is aligned to that of the middle layer.

Finally, to verify the performance of the proposed bifunctional metalens, a triple-layered prototype associated with the feeding LPDA is fabricated, assembled, and measured, as shown in Fig. 11. The three pieces of AM are sandwiched by foam spacers, whose relative permittivity and relative permeability are close to 1. The surroundings of far-field and near-field measurement are displayed in Fig. 11b, c, respectively. Besides, the scanning area of near field is 420 mm × 300 mm, which is sufficient to cover the entire lens system (marked by yellow rectangle), and the components of the tangential electrical fields on the metasurface are collected by a waveguide probe.

As described in Fig. 8, the proposed bifunctional metalens will function as a broadband Luneburg lens when the anisotropic metasurfaces are illuminated from *y* axis. The measured distributions of the instantaneous near electric field on the lens surface (*xoy*-plane) at 4, 6, and 8 GHz are compared with the numerical simulations successively, as demonstrated in Fig. 12. As can be seen from Fig. 12a–c, the measured electric-field distributions are in great agreement with the simulated ones, and the spherical waves radiated from the LPDA are dramatically transformed into quasi-plane waves, as predicted. To further reveal the performance of the metalens, the phase distributions of electric-field on *xoy*-plane are presented in Fig. 12d,e,f, as well. Likewise, it is obvious that the spherical wavefront can be converted to the quasi-planar wavefront in a broad band, and the effect of conversion is enhanced with the increase of frequency. For quantitative demonstration, simulated and measured gains versus frequency of the assembled tri-layered lens antenna (TLLA) and the feeding LPDA are plotted in Fig. 13. A significant gain enhancement can be observed from 2 to 8 GHz (relative bandwidth of 120%), which indicates a highly directional emission resulting from the Luneburg lens.

Attributing to the anisotropy of the metasurface, the bifunctional metalens will function as a wide-band Maxwell fisheye lens when we rotate it 90 degrees clockwise with the location of the LPDA fixed. The comparisons of the instantaneous near electric fields on *xoy*-plane at 5, 6, and 7 GHz are demonstrated in Fig. 14. The experimental measurements agree well with the numerical simulations. Both amplitude and phase distributions of electric field show that the radiation emitted from the LPDA is focused on the opposite periphery of the metalens, and then propagates as spherical waves in a band of 5 to 7 GHz (relative bandwidth of 33.3%).

In order to investigate the influence of cross-polarized electric fields on the performance of the bifunctional metalens, the simulated cross-polarized distributions of electric-field at 6 GHz for the Luneburg lens (E_y) and Maxwell fisheye lens (E_x) are illustrated in Fig. 15a,b, respectively. With respect to the TE-mode surface waves, the Poynting vector can be calculated as expression (5). According to the mechanism of the bifunctional metalens, the electric field E_x plays a dominant role in exciting the Luneburg lens, which is designed along *y*-axis. Similarly, the electric field E_y plays a dominant role in exciting the fisheye lens, which is designed along *x*-axis. Hence, it can be seen that the electric-field components of cross-polarization on the lens surface depicted in Fig. 15a,b are quite smaller than the corresponding components of co-polarization shown in Figs. 12 and 14. Moreover, compared with the theoretical predictions of beam path in Fig. 8, the power-density distributions in Fig. 15c,d show that the cross-polarized components of electric field do not much affect the power flows of the Luneburg and fisheye lenses as expected.

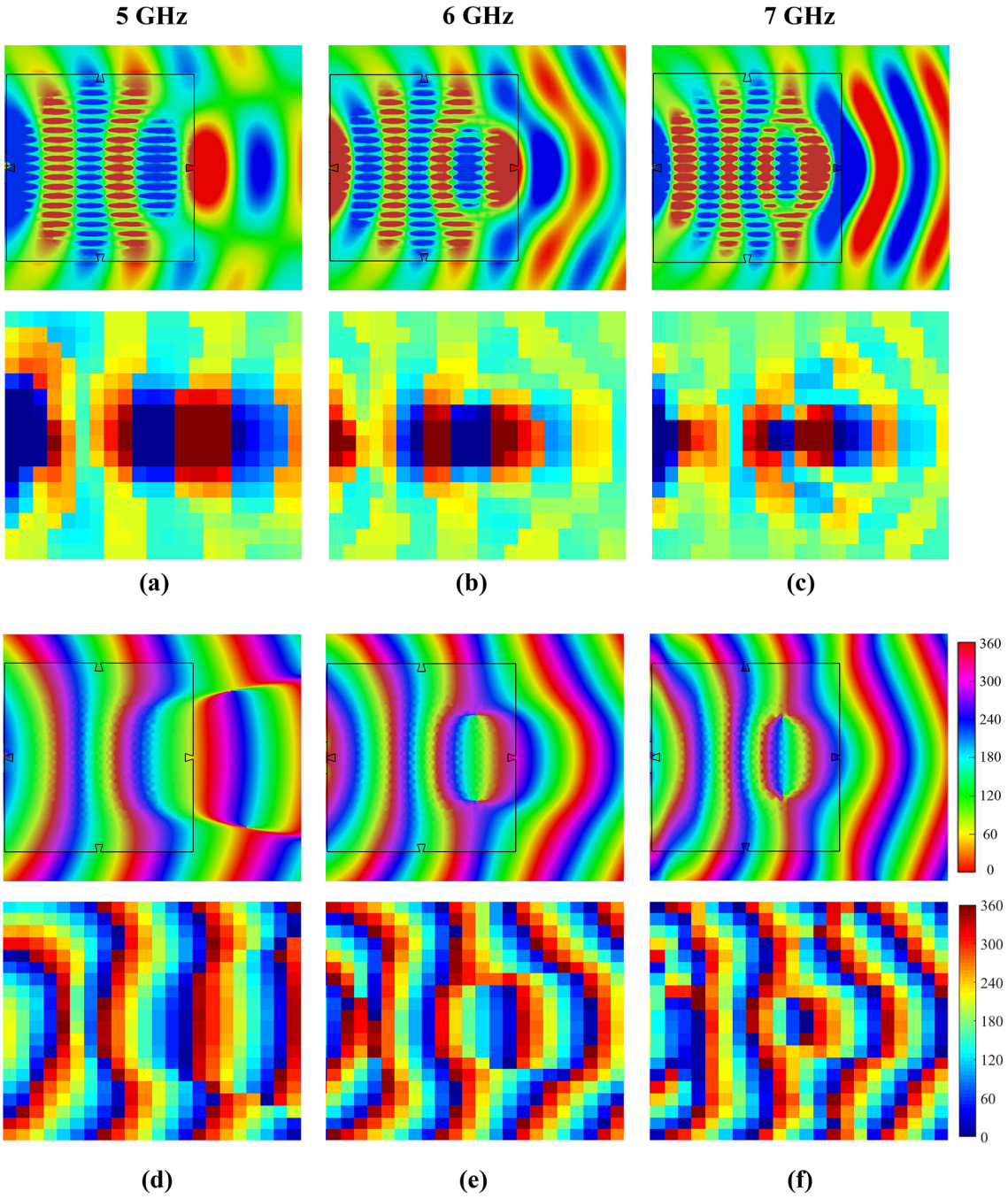

Figure 14. Comparisons of near electric-field distributions (E_y) on *xoy*-plane between the simulated results (upper part of each subgraph) and measured results (bottom part of each subgraph) at 5, 6, and 7 GHz when the proposed bifunctional metalens serves as a fisheye lens. (**a,b,c**) Amplitude distributions of simulated and measured electric field at 5, 6, and 7 GHz, respectively. (**d,e,f**) Phase distributions of simulated and measured electric field at 5, 6, and 7 GHz, respectively.

$$\vec{S} = E_y H_z \cdot \vec{e}_x + E_x H_z \cdot \vec{e}_y \tag{5}$$

Conclusions

A broadband bifunctional Luneburg-fisheye lens based on anisotropic metasurface is proposed. The planar bifunctional metalens is synthesized by non-resonant anisotropic cells with low profile, so that it can achieve distinctly inhomogeneous distributions of refractive index in orthogonal directions, respectively. By virtue of the anisotropy, the bifunctional metalens can serve as a broadband Luneburg lens observing from the horizontal

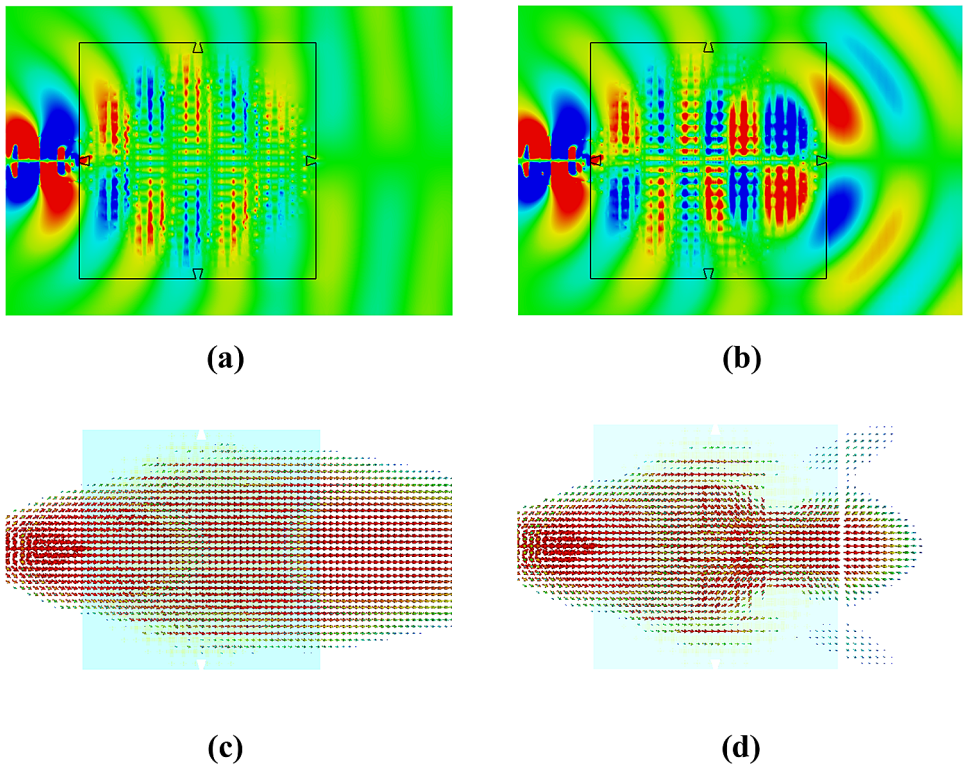

Figure 15. Simulated cross-polarized distributions of near electric-field regarding the bifunctional metalens on *xoy*-plane at 6 GHz. (**a**) The cross-polarized electric-field component (E_y) of Luneburg lens. (**b**) The cross-polarized electric-field component (E_x) of Maxwell fisheye lens. (**c**) Power-density distribution when illuminating from *y* axis (Luneburg lens). (**d**) Power-density of distribution when illuminating from *x* axis (fisheye lens).

axis in the frequency range of 2 to 8 GHz, while as a wide-band Maxwell fisheye lens observing from the vertical axis in the operating band of 5 to 7 GHz. What's more, our anisotropy-based approach is not only limited to an implementation of a Luneburg-fisheye lens, but can be flexibly applied to the realization of other broadband multifunctional metadevices operating in the region of microwave, optics, and even terahertz.

Received: 2 June 2020; Accepted: 9 November 2020
Published online: 23 November 2020

References

1. Chen, H. T., Taylor, A. J. & Yu, N. F. A review of metasurfaces: physics and applications. *Rep. Prog. Phys.* **79**(7), 076401 (2016).
2. Kildishev, A. V., Boltasseva, A. & Shalaev, V. M. Planar photonics with metasurfaces. *Science* **339**(6125), 1232009 (2013).
3. Cummer, S. A., Christensen, J. & Alu, A. Controlling sound with acoustic metamaterials. *Nat. Rev. Mater.* **1**(3), 16001 (2016).
4. Yu, N. F. *et al.* Light propagation with phase discontinuities: generalized laws of reflection and refraction. *Science* **334**(6054), 333–337 (2011).
5. Aieta, F. *et al.* Out-of-plane reflection and refraction of light by anisotropic optical antenna metasurfaces with phase discontinuities. *Nano Lett.* **12**(3), 1702–1706 (2012).
6. Jia, S. L., Wan, X., Bao, D., Zhao, Y. J. & Cui, T. J. Independent controls of orthogonally polarized transmitted waves using a Huygens metasurface. *Laser Photon. Rev.* **9**(5), 545–553 (2015).
7. Xu, H. X., Tang, S. W., Ling, X. H., Luo, W. J. & Zhou, L. Flexible control of highly-directive emissions based on bifunctional metasurfaces with low polarization cross-talking. *Ann. Phys.* **529**(5), 1700045 (2017).
8. Yang, H. H. *et al.* A programmable metasurface with dynamic polarization, scattering and focusing control. *Scientific Reports* **6**, 35692 (2016).
9. Faure, C., Richoux, O., Felix, S. & Pagneux, V. Experiments on metasurface carpet cloaking for audible acoustics. *Appl. Phys. Lett.* **108**(6), 064103 (2016).
10. Liu, S. *et al.* Anisotropic coding metamaterials and their powerful manipulation of differently polarized terahertz waves. *Light Sci. Appl.* **5**, e16076 (2016).
11. Xu, H. X., Liu, H. W., Ling, X. H., Sun, Y. M. & Yuan, F. Broadband vortex beam generation using multimode Pancharatnam-Berry metasurface. *IEEE Trans. Antennas Propag.* **65**(12), 7378–7382 (2017).
12. Yue, F. Y. *et al.* Vector vortex beam generation with a single plasmonic metasurface. *ACS Photon.* **3**(9), 1558–1563 (2016).
13. Erfani, E., Niroo-Jazi, M. & Tatu, S. A high-gain broadband gradient refractive index metasurface lens antenna. *IEEE Trans. Antennas Propag.* **64**(5), 1968–1973 (2016).
14. Guo, W. L. *et al.* Design of anisotropic focusing metasurface and its application for high-gain lens antenna. *J. Phys. D-Appl. Phys.* **50**(8), 085003 (2017).
15. Lin, Q. W. & Wong, H. A low-profile and wideband lens antenna based on high-refractive-index metasurface. *IEEE Trans. Antennas Propag.* **66**(11), 5764–5772 (2018).

16. Yang, Q. L. *et al.* Efficient flat metasurface lens for terahertz imaging. *Opt. Express* **22**(21), 25931–25939 (2014).
17. Singha, R. & Vakula, D. Directive beam of the monopole antenna using broadband gradient refractive index metamaterial for ultra-wideband application. *IEEE Access* **5**, 9757–9763 (2017).
18. Markovich, H., Filonov, D., Shishkin, I. & Ginzburg, P. Bifocal Fresnel lens based on the polarization-sensitive metasurface. *IEEE Trans. Antennas Propag.* **66**(5), 2650–2654 (2018).
19. Wang, H. F., Wang, Z. B., Cheng, Y. & Zhang, Y. R. Dual-polarized lens antenna based on multimode metasurfaces. *Chin. Phys. B* **27**(11), 118401 (2018).
20. Liu, K. T., Ge, Y. H. & Lin, C. X. A compact wideband high-gain metasurface-lens-corrected conical horn antenna. *IEEE Antennas Wirel. Propag. Lett.* **18**(3), 457–461 (2019).
21. Wan, X., Shen, X. P., Luo, Y. & Cui, T. J. Planar bifunctional Luneburg-fisheye lens made of an anisotropic metasurface. *Laser Photonics Rev.* **8**(5), 757–765 (2014).
22. Ma, H. F. & Cui, T. J. Three-dimensional broadband and broad-angle transformation-optics. *Nat. Commun.* **1**, 124 (2010).
23. Wu, L. L., Tian, X. Y., Yin, M., Li, D. C. & Tang, Y. P. Three-dimensional liquid flattened Luneburg lens with ultra-wide viewing angle and frequency band. *Appl. Phys. Lett.* **103**(8), 084102 (2013).
24. Ma, H. F. *et al.* Three-dimensional gradient-index materials and their applications in microwave lens antennas. *IEEE Trans. Antennas Propag.* **61**(5), 2561–2569 (2013).
25. Liang, M. *et al.* A 3-D Luneburg lens antenna fabricated by polymer jetting rapid prototyping. *IEEE Trans. Antennas Propag.* **62**(4), 1799–1807 (2014).
26. Xu, H. X., Wang, G. M., Tao, Z. & Cai, T. An octave-bandwidth half Maxwell fish-eye lens antenna using three-dimensional gradient-index fractal metamaterials. *IEEE Trans. Antennas Propag.* **62**(9), 4823–4828 (2014).
27. Dockrey, J. A. *et al.* Thin metamaterial Luneburg lens for surface waves. *Phys. Rev. B* **87**(12), 125137 (2013).
28. Dhouibi, A., Burokur, S. N., de Lustrac, A. & Priou, A. Metamaterial-based half Maxwell fish-eye lens for broadband directive emissions. *Appl. Phys. Lett.* **102**(2), 024102 (2013).
29. Wan, X., Jiang, W. X., Ma, H. F. & Cui, T. J. A broadband transformation-optics metasurface lens. *Appl. Phys. Lett.* **104**(15), 151601 (2014).
30. Shi, Y., Li, K., Wang, J., Li, L. & Liang, C. H. An etched planar metasurface half Maxwell fish-eye lens antenna. *IEEE Trans. Antennas Propag.* **6**(8), 3742–3747 (2015).
31. Chen, K. C., Yang, J. W., Yang, Y. C., Khin, C. F. & Kehn, M. N. M. Plasmonic Luneburg lens antenna synthesized by metasurfaces with hexagonal lattices. *Opt. Express* **25**(22), 27405–27414 (2017).
32. Chou, H. C., Tung, N. L. & Kehn, M. N. M. The double-focus generalized Luneburg lens design and synthesis using metasurfaces. *IEEE Trans. Antennas Propag.* **66**(9), 4936–4941 (2018).
33. Ma, H. F., Wang, G. Z., Kong, G. S. & Cui, T. J. Independent controls of differently-polarized reflected waves by anisotropic metasurfaces. *Sci. Reports* **5**, 9605 (2015).
34. Zhu, R. R. *et al.* Bifunctional acoustic metamaterial lens designed with coordinate transformation. *Appl. Phys. Lett.* **110**(11), 113503 (2017).
35. Lu, H. D. *et al.* Fully metallic anisotropic lens crossover-in-antenna based on parallel plate waveguide loaded with uniform posts. *IEEE Trans. Antennas Propag.* **68**(7), 5061–5070 (2020).
36. Li, J. S. & Pendry, J. B. Hiding under the Carpet: a new strategy for cloaking. *Phys. Rev. Lett.* **101**(20), 203901 (2008).
37. Chen, X. D., Grzegorczyk, T. M., Wu, B. I., Pacheco, J. & Kong, J. A. Robust method to retrieve the constitutive effective parameters of metamaterials. *Phys. Rev. E* **70**(1), 016608 (2004).
38. Liu, R. P., Cui, T. J., Huang, D., Zhao, B. & Smith, D. R. Description and explanation of electromagnetic behaviors in artificial metamaterials based on effective medium theory. *Phys. Rev. E* **76**, 026606 (2007).
39. Smith, D. R., Vier, D. C., Koschny, T. & Soukoulis, C. M. Electromagnetic parameter retrieval from inhomogeneous metamaterials. *Phys. Rev. E* **71**(3), 036617 (2005).

Acknowledgements

This work was supported in part by the National Natural Science Foundation of China (61601219) and Nature Science Foundation of Jiangsu Province (BK20160804).

Authors contributions

J.Q. Chen conceived the idea and performed the numerical simulations. J.Q. Chen, Y. J. Zhao, and L. Xing conducted the theoretical analyses. J.Q. Chen, Z. He, and L.Y. Sun did the measurements. J. Q. Chen wrote the manuscript, and all authors contributing to the manuscript review.

Competing interests

The authors declare no competing interests.

Additional information

Correspondence and requests for materials should be addressed to J.C. or Y.Z.

Reprints and permissions information is available at www.nature.com/reprints.

Publisher's note Springer Nature remains neutral with regard to jurisdictional claims in published maps and institutional affiliations.

Open Access This article is licensed under a Creative Commons Attribution 4.0 International License, which permits use, sharing, adaptation, distribution and reproduction in any medium or format, as long as you give appropriate credit to the original author(s) and the source, provide a link to the Creative Commons licence, and indicate if changes were made. The images or other third party material in this article are included in the article's Creative Commons licence, unless indicated otherwise in a credit line to the material. If material is not included in the article's Creative Commons licence and your intended use is not permitted by statutory regulation or exceeds the permitted use, you will need to obtain permission directly from the copyright holder. To view a copy of this licence, visit http://creativecommons.org/licenses/by/4.0/.

© The Author(s) 2020